

Wiener Filtering Improves Quantification of Regional Myocardial Perfusion with Thallium-201 SPECT

Jonathan M. Links, Richmond W. Jeremy*, Stephen M. Dyer, Terry L. Frank, and Lewis C. Becker

Division of Cardiology, Department of Medicine, and the Division of Nuclear Medicine, Department of Radiology, The Johns Hopkins Medical Institutions, Baltimore, Maryland

Quantitation of myocardial perfusion with thallium-201 (^{201}Tl) SPECT is limited by finite resolution and image noise. This study examined whether Wiener filtering could improve quantitation of the severity of myocardial perfusion deficits. In 19 anesthetized dogs, adjustable stenoses were placed on the left anterior descending (LAD, $n=12$) or circumflex (LCx, $n=7$) arteries. Thallium-201 SPECT images were acquired during maximal coronary vasodilation with dipyridamole, and simultaneous measurements of myocardial blood flow were made with microspheres. The relationship between SPECT and microsphere flow deficits in the LAD region was significantly better ($p<0.05$) with Wiener filtering ($Y=0.90X + 0.03$, $r=0.78$) than with conventional Hanning filtering ($Y=0.66X + 0.34$, $r=0.61$). Similarly, in the LCx region the relationship between SPECT and microsphere perfusion deficits was better ($p<0.01$) with the Wiener filter ($Y=0.91X + 0.07$, $r=0.66$) than with the Hanning filter ($Y=0.36X + 0.50$, $r=0.40$). Wiener filtering improves quantitation of the severity of regional myocardial perfusion deficits, allowing better assessment of the functional significance of coronary artery stenoses.

J Nucl Med 1990; 31:1230-1236

Radionuclide imaging, using either planar or tomographic techniques, is a principle means for clinical evaluation of regional myocardial perfusion. Radionuclide images are, however, characterized by both limited spatial resolution and high levels of statistical noise, which confound quantitation of regional myocardial perfusion. Conventional methods to reduce noise, such as local weighted averaging, produce further deterioration in spatial resolution, while the use of

deconvolution to recover resolution typically amplifies noise to unacceptable levels (1).

Several groups of investigators have described the use of "optimized" two-dimensional Fourier filters (2-9), which seek to simultaneously recover resolution and reduce noise. These filters have been applied to planar imaging of the liver (2) and heart (4) and single-photon emission computed tomography (SPECT) imaging of the brain (6-8), skeleton (6,8), liver (7,8) and heart (8). In these studies, the benefits of the filtering were judged by either subjective improvement in "image quality" (6-8), or quantitative receiver operating characteristic (ROC) analysis of visual interpretation performance (2-4,9). The use of such "optimized filters" holds the promise of improved quantitation of myocardial perfusion. This study examined the effects of Wiener filtering of thallium SPECT projection data prior to reconstruction on quantitation of myocardial perfusion deficits in dogs with experimental coronary stenoses of mild to moderate severity. The severity of perfusion deficit, calculated from the SPECT data was compared with direct microsphere measurements of perfusion deficit in each dog.

MATERIALS AND METHODS

Experimental Preparation

Nineteen mongrel dogs (20-25 kg) were anesthetized with thiamylal sodium (12.5 mg/kg IV) and chloralose (14 mg/kg) in urethane (136 mg/kg IM). The dogs were ventilated with room air and supplementary oxygen (21/min). Catheters were inserted into the right femoral vein for injection of radionuclide tracers and into the right femoral artery for measurement of systemic arterial pressure and for withdrawal of reference microsphere samples. After a left thoracotomy, a polyvinyl catheter was placed in the left atrium for microsphere injection. The proximal left anterior descending (LAD) ($n = 12$) or circumflex (LCx) ($n = 7$) artery was exposed and a calibrated electromagnetic flow probe placed around the artery. The coronary flow signal was analyzed by a sine-wave flowmeter (Biotronix BL-613, Kensington MD) and coronary flow and arterial pressure were recorded on chart paper (Gould Brush 200).

Received Apr. 13, 1989; revision accepted Feb. 5, 1990.
For reprints contact: Jonathan M. Links, PhD, Division of Nuclear Medicine, Johns Hopkins Medical Institutions, 615 N. Wolfe St., Baltimore, MD 21205-2179.

* Dr. Jeremy is an Overseas Research Fellow of the National Heart Foundation of Australia and recipient of a Teletronics Travelling Fellowship from the Royal Australasian College of Physicians.

A plastic screw clamp was also placed around the coronary artery, just distal to the flow probe, and seated so as not to kink the artery. The clamp was then adjusted to cause mild to moderate reduction in the magnitude of peak hyperemic flow following a 15-sec coronary occlusion. The clamp was not tight enough to impede resting coronary flow in any dog. After adjustment of the clamp, the flow probe was removed and the heart replaced within the pericardial sac. The chest was then closed in layers and the left atrial catheter brought to the skin surface.

Single-Photon Emission Computed Tomography

Each dog was placed on the imaging table in a lateral position, with the right side down. Coronary vasodilation was then induced by intravenous infusion of dipyridamole (Persantine, Boehringer Ingelheim, Inc.) at 0.142 mg/kg/min for 3 min. The infusion was then reduced to a maintenance rate of 0.014 mg/kg/min for the remainder of the study (10,11). One minute after the reduction in the infusion rate of dipyridamole, 2–3 mCi of thallium-201 (^{201}Tl) were injected intravenously and a simultaneous injection of 2 million radio-nuclide-labeled microspheres (iodine-125 or gadolinium-153) was made into the left atrium. A reference blood sample was simultaneously withdrawn from the femoral artery at a rate of 2.16 ml/min, commencing 1 min before the left atrial injection of microspheres.

Acquisition of the projection images began 5 min after the ^{201}Tl injection. A rotating Technicare Omega 500 rectangular field-of-view camera, with a low-energy, high-resolution collimator was employed, with a 20% energy window placed over the ^{201}Tl photopeak. Images were acquired in a 128×128 frame mode, with a 2× zoom. Thirty projection images were acquired over a 180-degree arc from right lateral to anterior to left lateral positions, with a 60-sec acquisition time for each image.

At the conclusion of the study, the dog received a lethal dose of KCl and the heart was excised and fixed in 10% formalin. The right ventricle, atria, epicardial fat and great vessels were removed before the left ventricle was sectioned into five transverse slices of 8–10 mm thickness. Each of the transverse slices was then divided into 12 radial sections, which were individually counted in a well spectrometer (Packard Model 5986), with correction for radionuclide decay. Regional blood flow in each sample was then calculated according to the reference organ technique (12) as:

$$Q_m = (C_m \cdot Q_r) / (C_r \cdot W_m),$$

where Q_m = myocardial blood flow, C_m = corrected myocardial cts/min, Q_r = reference sample withdrawal rate, C_r = reference sample cts/min, and W_m = weight of the myocardial sample. The severity of a regional perfusion deficit in each slice was calculated as the ratio Q_d/Q_n , where Q_d was the lowest flow in any one radial section and Q_n was the flow in a section 180° opposite within the same myocardial slice (13).

Image Reconstruction

The SPECT projection images were corrected for nonuniformities with a 120-million count flood and for center-of-rotation variations with a line-source calibration. No attenuation or scatter correction was employed. The myocardial image data was isolated from background structures by a circular region of interest, which excluded non-cardiac activity

(such as hepatic) that could distort the image power spectrum. The projection data were then reconstructed in two different ways:

1. Using our standard approach, which involves no pre-reconstruction filtering, and a Hanning reconstruction filter with a cut-off of 0.29 Nyquist. We have previously validated the use of this filter, which results in an effective reconstructed resolution of 2.5 cm, in a large series of patient studies (14).
2. Using Wiener filtering of the projection data, prior to reconstruction with a ramp filter. The data were initially reconstructed into contiguous 3-pixel thick (6.5 mm) transverse slices. The contiguous transverse data were then reoriented into 3-pixel thick short-axis, vertical long-axis and horizontal long-axis slices, with the reference ventricular axes being defined by the operator on the display of transverse and oblique sagittal data.

Description of Wiener Filter

The Wiener filter is a two-dimensional Fourier space filter, the design and use of which is based upon the following assumptions: (1) the imaging system is linear and stationary, (2) the noise is additive with constant variance and is not correlated with the object, and (3) the “optimized” filter is that which minimizes the mean-square error between the original object and the filtered image. Given these assumptions, the Wiener filter (in one dimension) is described by:

$$W(f) = \text{MTF}^{-1} \times \text{MTF}^2 / (\text{MTF}^2 + N/O), \quad (1)$$

where $W(f)$ is the value of the filter as a function of spatial frequency, MTF is the modulation transfer function of the imaging system, N is the noise power spectrum, and O is the object power spectrum. The equation is specifically written in this form to emphasize the two functions of the filter: resolution recovery as the inverse of the MTF, and noise reduction as a low-pass filter with a roll-off dependent on the relationship between image noise and signal (the object as passed through the imaging system's MTF).

For implementation of the Wiener filter, the MTF of the imaging system must be known a priori, and N and O must be determined from the image to be filtered. We obtained a one-dimensional MTF from annular averaging of the two-dimensional Fourier transform of an image of a point source for our camera/collimator system, with the point source at a depth of 10 cm in water, and with an additional 3 cm of air between the surface of the phantom and the collimator. In practice, it was necessary to threshold the image of the point source (to zero all pixels whose value was <2% of the maximum pixel value) in order to eliminate extraneous image noise distant from the source, the presence of which resulted in high frequency artifacts in the calculated MTF. We estimated the noise in the image by assuming that: (1) the noise was “white” (constant over all frequencies), and (2) the image power at the frequencies where the MTF was very low represented noise alone. We therefore averaged the image power spectrum values over those high frequencies after the MTF had decreased to 0.05, and this average value was designated as N , independent of frequency, in Equation 1. Like King and coworkers (3), we assumed that the image power spectrum

was the object power spectrum modified by the MTF, with constant noise added:

$$I = (O \times \text{MTF}^2) + N \quad (2)$$

The object power spectrum was then estimated by rearranging Equation 2 and solving for O . The Wiener filter was designed one-dimensionally, and then "spun" to generate a two-dimensional, circularly symmetric filter. The filter was designed using the anterior image in a given study; the same filter was then applied to every projection image in that study.

Image Analysis

After reconstruction, the images were displayed on a video monitor and reviewed for the presence and location of any perfusion defect by a blinded observer. The observer identified the three short-axis slices which best passed through a perfusion defect and these were used for analysis. A circular region of interest was placed around the outer edge of each myocardial slice and 120 radii then projected from the center of the circular region to the outer myocardial border. Circumferential profiles, which recorded the maximum pixel value along each radius, were generated in 3-degree steps for each of the 3 short-axis image slices. In each slice, the radius with the lowest pixel value was identified and compared with the radius value in the region 180° opposite, to obtain a ratio C_d/C_n , where C_d = maximum pixel value in the perfusion defect and C_n = maximum pixel value in the normal region (13). The same analysis was applied to both the Hanning and Wiener filtered images.

Statistical Analysis

The most apical and basal myocardial slices were eliminated and the microsphere data for the middle three myocardial slices compared with the corresponding three SPECT image slices. The relationship between severity of perfusion defect measured by microspheres and severity measured by ^{201}Tl SPECT was determined by linear regression for both the Wiener and Hanning filtered images and the linear regressions for each filter were compared by analysis of covariance (15). Results are expressed as mean \pm standard deviation (s.d.) and a p value <0.05 is regarded as significant.

RESULTS

Mean aortic pressure before dipyridamole infusion was 102 ± 17 mmHg and after dipyridamole was 93 ± 23 mmHg. Mean coronary flow in the normal regions of myocardium, measured by microspheres after dipyridamole infusion, was 5.2 ± 2.7 ml/min/g, indicating near maximal coronary vasodilation induced by dipyridamole.

Representative examples of images for perfusion defects in the left anterior descending and circumflex territories are shown for the Hanning and Wiener filters in Figures 1 and 2. In the LAD artery example, a perfusion defect is evident involving the apex and anterior free wall (Fig. 1). The Wiener filter image exhibits sharper edge definition and better contrast between the normal and ischemic regions. The Hanning filter image appears more blurred, with markedly less definition of the perfusion defect, and obscuration of the ventricular

HANNING FILTER



WIENER FILTER

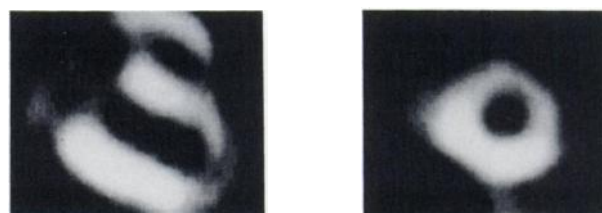
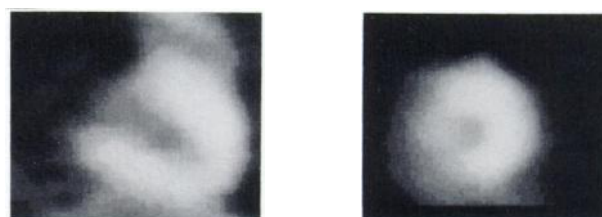


FIGURE 1
Representative example of a myocardial perfusion deficit in the LAD territory. Short-axis and vertical long-axis images are displayed after processing with either a Hanning or a Wiener filter. Improved image contrast and clearer definition of the perfusion deficit is evident with the Wiener filter.

cavity. The perfusion deficit, measured by microspheres, was 47% of the control region in this study. In the circumflex artery example (Fig. 2), a perfusion deficit is evident in the posterolateral left ventricular free wall. The microsphere perfusion deficit, measured

HANNING FILTER



WIENER FILTER



FIGURE 2
Representative example of a myocardial perfusion deficit in the circumflex territory. Short-axis and vertical long-axis images are displayed after processing with either a Hanning or a Wiener filter. Improved definition of the perfusion deficit is again observed with the Wiener filter.

by microspheres, was 49% of control in this study. Again, clearer images and better contrast between the normal and ischemic myocardium is obtained with use of the Wiener filter.

The relationship between regional perfusion deficits measured by microspheres and ^{201}Tl SPECT in each of the middle three slices of the left ventricle is shown for the Hanning filter in Figure 3 and for the Wiener filter in Figure 4. There was a poor relationship between microsphere and ^{201}Tl perfusion deficits with Hanning filtering ($Y = 0.60X + 0.37$, $r = 0.57$, $\text{s.e.e.} = 0.13$), with a decided tendency for the ^{201}Tl images to underestimate the degree of the more severe perfusion deficits. The relationship between microsphere and ^{201}Tl perfusion deficits was improved with Wiener filtering ($Y = 0.88X + 0.05$, $r = 0.74$, $\text{s.e.e.} = 0.12$). This relation differed from that for the Hanning filter ($p < 0.01$) but did not differ significantly from the line of identity. The small intercept value was also not significantly different from zero.

The relationships between microsphere and ^{201}Tl perfusion deficits in the LAD territory are compared for the Hanning and Wiener filter images in Figure 5. The close relationship for the Wiener filtered images ($Y = 0.90X + 0.03$, $r = 0.78$, $\text{s.e.e.} = 0.13$) did not differ from the line of identity, and was better ($p < 0.05$) than the relationship for the Hanning filtered images ($Y = 0.66X + 0.34$, $r = 0.61$, $\text{s.e.e.} = 0.15$). The same comparison between microsphere and ^{201}Tl perfusion deficits in the circumflex territory is illustrated in Figure 6. As with the LAD territory, the relationship between microsphere and the Wiener filtered ^{201}Tl perfusion deficits ($Y = 0.91X + 0.07$, $r = 0.66$, $\text{s.e.e.} = 0.11$) followed the line of identity. In contrast, there was again a poor relationship between the microsphere and Hanning filtered ^{201}Tl perfusion deficits ($Y = 0.36X + 0.50$, $r = 0.40$, $\text{s.e.e.} = 0.09$), which was significantly different from the Wiener filter relationship ($p < 0.01$).

DISCUSSION

The physical limitations of nuclear imaging result in images with markedly inferior spatial resolution and higher noise levels compared to other medical imaging techniques. Until recently, major emphasis was placed on developing instrumentation with a combination of better resolution and higher sensitivity as a means of improving image quality. Digital processing of data has also been employed in attempts to improve image quality (1,16,17). Unfortunately, most conventional digital filtering approaches in nuclear medicine improve either resolution or noise only at the expense of the other.

More sophisticated filters have been available for some years (1), but the speed of commercial computer systems prevented their use in a clinical setting. With the advent of array processor hardware (18), the ex-

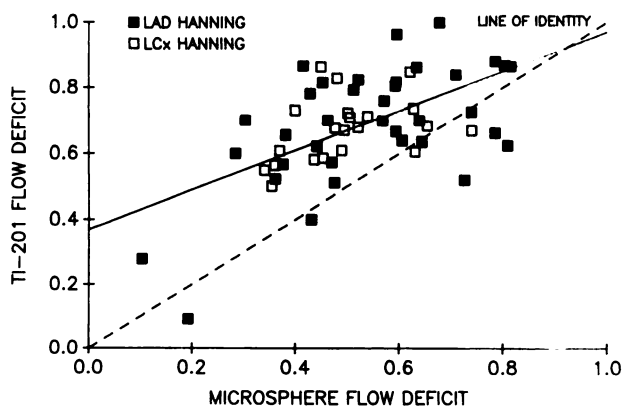


FIGURE 3

The relationship between regional microsphere flow deficit and the ^{201}Tl flow deficit for images processed with the Hanning filter ($Y = 0.60X + 0.37$, $r = 0.57$, $\text{s.e.e.} = 0.13$). Data is shown for each of three contiguous short-axis myocardial slices which include the perfusion deficit. Data for both anterior descending (LAD) and circumflex (LCx) stenoses are shown. The line of identity is shown by the dashed line.

cution time for two-dimensional Fourier filtering has decreased to the point where it is now feasible to consider its routine use. Indeed, most of the reports of more advanced image filtering have followed the introduction of array processors into nuclear medicine systems (2-9).

These reports have described filters which simultaneously recover resolution and reduce noise. These filters are based on one of three relationships: the Metz (2,5,7-9), the Wiener (3-5) or the Gaussian (6), each of which has a similar underlying spatial frequency response. The filters start with a response value of 1.0 at the "zero" frequency (for unity gain), the response increases above 1.0 at low to intermediate spatial fre-

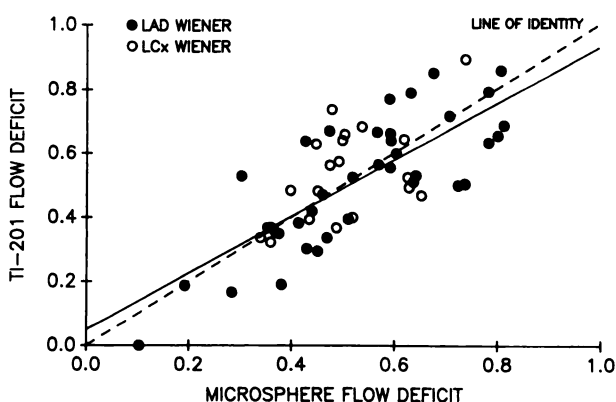


FIGURE 4

The relationship between regional microsphere flow deficit and the ^{201}Tl flow deficit for images processed with the Wiener filter ($Y = 0.88X + 0.05$, $r = 0.74$, $\text{s.e.e.} = 0.12$). Data is shown for each of three contiguous short-axis myocardial slices which include the perfusion deficit. Data are shown for both anterior descending (LAD) and circumflex (LCx) coronary stenoses. The line of identity is shown as a dashed line.

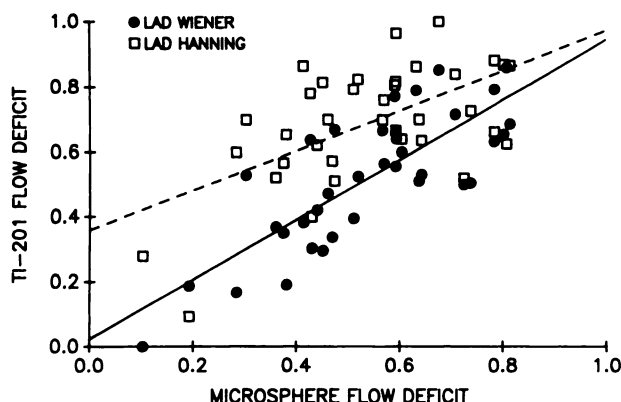


FIGURE 5

Comparison of the relationships between regional microsphere flow deficit and the thallium-201 flow deficit in the anterior descending (LAD) territory for images processed with the Hanning filter ($Y = 0.66X + 0.34$, $r = 0.61$, s.e.e. = 0.15, dashed line) and the Wiener filter ($Y = 0.90X + 0.03$, $r = 0.78$, s.e.e. = 0.13, solid line).

quencies (for resolution recovery) and then "rolls-off" down to zero at high spatial frequencies (for noise reduction). The actual shape of each filter differs because of the approach used to define it. The Metz filter, which is of the form:

$$M(f) = MTF^{-1} \times (1 - (1 - MTF^2)^x) \quad (3)$$

is designed, like the Wiener filter, to minimize the mean square difference between the original object and the filtered image. Its generation requires a priori knowledge of the actual object in order to determine the "optimal" 'x' in Equation 3, and King and coworkers (2) chose to use a phantom for derivation of their Metz filter. The Metz filter can be made more image dependent by making 'x' a function of total image counts, or

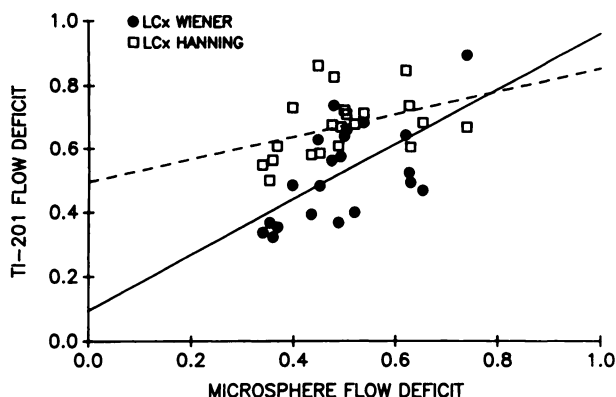


FIGURE 6

Comparison of the relationships between regional microsphere flow deficit and the ^{201}Tl flow deficit in the circumflex (LCx) territory for images processed with the Hanning filter ($Y = 0.36X + 0.50$, $r = 0.40$, s.e.e. = 0.09, dashed line) and the Wiener filter ($Y = 0.91X + 0.07$, $r = 0.66$, s.e.e. = 0.11, solid line).

by putting constraints on its derivation and adjusting the parameters via a predetermined regression relationship (19). We chose to use the Wiener filter instead, because it does not require any a priori assumptions about the composition of the object. Like Madsen and coworkers (6), we have noted striking improvements in subjective image quality with even an arbitrarily shaped Gaussian filter, but we chose to explicitly correct for blurring effects with the inverse of the MTF, as the Wiener filter provides, and to more objectively determine the optimum frequency to begin noise reduction.

The Wiener filters used in this study, derived from the MTF of the imaging system and the power spectrum of the cardiac image in each dog, appeared to improve defect quantification by both scatter reduction (assessed by the full width at tenth maximum, FWTM) and resolution recovery (assessed by the full width at half maximum, FWHM). Phantom studies (see Appendix) indicated an improvement in both the FWTM and the FWHM of the reconstructed point spread function with application of the Wiener filter compared to use of the Hanning filter (FWTM: 29.2 versus 39.5 mm; FWHM: 16.6 versus 21.0 mm).

A single filter was employed for all projections in a given study, in order to reduce the time requirements for design of the filter and to ensure that the projection data remained consistent after filtering. Nonetheless, the filter was individually "optimized" for each SPECT study. While the image power spectra from the present dog studies were similar, we have observed significant variations between patient studies, reflecting differing pathology and body habitus. In addition, the filter was implemented in Fourier space rather than real space. Miller and Sampathkumaran (17) have suggested that a convolution kernel (for real-space filtering) of 9×9 represents a good compromise between filter accuracy and execution time. On our system, such a convolution operation would take longer than two-dimensional Fourier filtering, and we also considered that Fourier space operations yielded more accurate results.

Like King and coworkers (5), we prefer to filter the projection data, rather than the reconstructed images. Firstly, the noise power spectrum in the projection images can be assumed to be Poisson in nature, because it has not yet been amplified or modified by the reconstruction process (20). Secondly, two-dimensional filtering of the projection data utilizes the entire data set in the filtering process. Finally, projection filtering followed by reconstruction with a ramp filter tends to preserve isotropic spatial resolution (5). It is interesting to note that the benefits of projection data filtering are not limited to filtered backprojection reconstruction (21).

We chose to examine the effects of Wiener filtering using a model of coronary stenoses of mild-moderate severity. Maximal coronary vasodilation was induced

by dipyridamole, and the present measurements reflect the functional significance of the stenosis according to the relative reductions in maximal coronary flow. The myocardium in the region of the perfusion deficit was not ischemic, however, as the stenoses did not impede resting coronary flow. Clinically, quantitation of perfusion deficits would be useful in assessment of the functional importance of coronary stenoses which appear to be of 'mild-moderate' severity on coronary angiography.

A limitation of thallium imaging is that, in patients with multi-vessel coronary disease, myocardium perfused by a mildly stenosed artery may appear normal relative to myocardium perfused by a severely stenosed artery. In this setting, the ratio of pixel values in the most severe perfusion deficit to that in an apparently normal region would underestimate the actual flow reduction to the more severely stenosed region. We chose to use an experimental model with only single vessel stenosis, and thus we could assume that the region 180° opposite the perfusion deficit represented normally perfused myocardium. In practice, it may be preferable to take the highest count region as 'normal' on the assumption that it is unlikely that the entire myocardium will have reduced coronary flow.

There are several considerations which affect the extension of the present findings to studies in human subjects. The statistical nature of the distribution of a finite number of microspheres and difficulties in directly matching ex vivo tissue samples with their corresponding SPECT image regions may well have limited the observed correlation between microsphere and thallium perfusion deficits. In addition, the smaller size of the canine heart, compared with the human heart, may be associated with reduced image resolution. On the other hand, the more central position of the canine heart within the thorax may minimize nonuniform attenuation effects, which may be greater with the more eccentric location of the human heart.

Despite the preponderance of computers in nuclear medicine, many studies are still subjectively interpreted by observers. Thus, assessment of the utility of advanced digital filtering has been limited to quantitation of improvements in observer accuracy (2-4,9). With the advent of automated computer quantitation programs, particularly for thallium-201 studies (22,23), quantitative accuracy has assumed equal importance to subjective image quality. This study demonstrates that application of the Wiener filter prior to reconstruction of ²⁰¹Tl SPECT images improves the accuracy of quantitation of regional myocardial perfusion deficits. As a result, the Wiener filter is routinely used for clinical ²⁰¹Tl SPECT studies in our department.

APPENDIX

Characterization of the effects of the Wiener filter was performed with phantom studies to separately examine reso-

lution recovery, scatter correction and noise reduction. To assess resolution and scatter, thallium point sources were imaged in air and in a 20-cm diameter cylinder filled with nonradioactive water. Four different Wiener filters were initially generated: air MTF/air point source image, air MTF/water point source image, water MTF/air point source image, and water MTF/water point source image. These filters were based on the characteristics of the individual point source images. For comparison of the in vivo filters, an "average" dog filter was generated by averaging the Wiener filters from the individual dog studies. In fact, there was little variation in filter characteristics between dogs, because of the standardized methods employed in image acquisition. These five different Wiener filters, plus ramp-only reconstruction, and the standard Hanning filter, were each applied to SPECT studies of the point sources, and the FWHM and FWTM of the point spread functions were measured (Table A1).

In initial planar images, the original (unfiltered) FWHM and FWTM were lower in air than in water. Application of the average dog Wiener filter resulted in a small increase in the planar FWHM, but a decrease in the FWTM, which was particularly evident in the water phantom. In the SPECT images, the original (ramp only) FWHM was essentially equivalent in air and water media, with a larger FWTM in water due to scatter effects. All four of the Wiener filters derived from the point source images produced similar results, with an improvement in both FWHM and FWTM over ramp-only reconstruction. The point source images had essentially the same total number of counts as the dog studies, but the object and image power spectra were different. The point source images had significantly greater high-frequency power, resulting in Wiener filters which rolled-over at higher frequencies than did the dog filters. This resulted in improved resolution recovery (lower FWHM) and scatter reduction (lower FWTM). The average dog filter FWHM was greater than the FWHM with ramp-only reconstruction, but the FWTM in a water medium was over 3 mm better with Wiener filtering

TABLE A1
Point-Source Functions in Air and Water

Filter	Point source in air		Point source in water	
	FWHM	FWTM (mm)	FWHM	FWTM (mm)
Original planar	12.0	22.5	13.7	26.1
Dog	13.7	22.2	14.4	23.4
Wiener planar				
Ramp-Only	14.1	26.2	14.7	32.5
SPECT				
Hanning	20.5	37.0	21.0	39.5
SPECT				
Dog	16.3	28.7	16.6	29.2
Wiener SPECT				
Air MTF	12.8	21.1	12.6	22.9
Point Source				
Wiener SPECT				
Water MTF	12.8	21.1	12.9	23.1
Point Source				
Wiener SPECT				

than with ramp-only reconstruction. This is consistent with greater scatter reduction by the Wiener filter. Application of the dog Wiener filter resulted in a FWHM of 4 mm less than did the Hanning filter and a FWTM of 10 mm less. Thus, the Wiener filters employed in the dog studies produced both scatter reduction and improved resolution, in comparison with the Hanning filter.

The effects of the Wiener filter on noise reduction were assessed with a SPECT study of a 20 cm diameter cylinder, uniformly filled with thallium in water. The total image counts in this study were equivalent to those of the dog studies (~30,000 counts/projection). The pixel-to-pixel coefficient of variation (standard deviation/mean) was measured within a large, square region of interest in a transverse slice, which was reconstructed with ramp-only filtering, the average dog Wiener filter and the Hanning filter. The coefficient of variation was 60% with ramp-only filtering, 35% with Wiener filtering and 10% with Hanning filtering. Thus the Wiener filter reduced the noise compared to ramp filtering, but the Hanning filter, with a much lower frequency roll-off, was associated with even greater noise reduction.

ACKNOWLEDGMENTS

The authors wish to thank Mr. Alexander Wright and Mr. Anthony Di Paula for their expert technical assistance.

Supported by U.S. Public Health Service grant No. 17655 (SCOR in Ischemic Heart Disease) from the National Institutes of Health, Bethesda, MD, and by a gift from Mary L. Smith of the W.W. Smith Charitable Trust, Rosemont, PA.

REFERENCES

1. Todd-Pokropek A. Image processing in nuclear medicine. *IEEE Trans Nucl Sci* 1980; NS-27:1080-1094.
2. King MA, Doherty PW, Schwinger RB, Jacobs DA, Kidder RE, Miller TR. Fast count-dependent digital filtering of nuclear medicine images. *J Nucl Med* 1983; 24:1039-1045.
3. King MA, Doherty PW, Schwinger RB. A Wiener filter for nuclear medicine images. *Med Phys* 1983; 10:876-880.
4. Miller TR, Goldman KJ, Epstein DM, et al. Improved interpretation of gated cardiac images by use of digital filters. *Radiology* 1984; 152:795-800.
5. King MA, Schwinger RB, Doherty PW, Penney BC. Two-dimensional filtering of SPECT images using the Metz and Wiener filters. *J Nucl Med* 1984; 25:1234-1240.
6. Madsen MT, Park CH. Enhancement of SPECT images by Fourier filtering of the projection image set. *J Nucl Med* 1985; 26:395-402.
7. King MA, Schwinger RB, Penney BC, Doherty PW, Bianco JA. Digital restoration of indium-111 and iodine-123 SPECT images with optimized Metz filters. *J Nucl Med* 1986; 27:1327-1336.
8. King MA, Glick SJ, Penney BC, Schwinger RB, Doherty PW. Interactive visual optimization of SPECT prereconstruction filtering. *J Nucl Med* 1987; 28:1192-1198.
9. Gilland DR, Tsui BMW, McCartney WH, Perry JR, Berg J. Determination of the optimum filter function for SPECT imaging. *J Nucl Med* 1988; 29:643-650.
10. Gould KL. Pharmacological intervention as an alternative to exercise stress. *Semin Nucl Med* 1987; 17:121-130.
11. Gould KL, Westcott RJ, Albro PC, Hamilton GW. Noninvasive assessment of coronary stenoses by myocardial imaging during pharmacologic vasodilation. II. Clinical methodology and feasibility. *Am J Cardiol* 1978; 41:279-287.
12. Heymann MA, Payne BD, Hoffman JI, Rudolph M. Blood flow measurements with radionuclide labelled particles. *Prog Cardiovasc Dis* 1977; 20:50-79.
13. Li Q-S, Frank TL, Franceschi D, Wagner HN Jr, Becker LC. Technetium-99m methoxyisobutyl isonitrile (RP30) for quantification of myocardial ischemia and reperfusion in dogs. *J Nucl Med* 1988; 29:1539-1548.
14. Fintel DF, Links JM, Brinker JA, Frank TL, Parker M, Becker LC. Improved diagnostic performance of exercise thallium-201 single photon emission computed tomography over planar imaging in the diagnosis of coronary artery disease: a receiver operating characteristic analysis. *J Am Coll Cardiol* 1989; 13:600-612.
15. Glantz SA. *Primer of biostatistics*, 2nd edition. New York: McGraw-Hill; 1987: 211-220.
16. Miller TR, Sampathkumaran KS. Digital filtering in nuclear medicine. *J Nucl Med* 1982; 23:66-72.
17. Miller TR, Sampathkumaran KS. Design and application of finite impulse response digital filters. *Eur J Nucl Med* 1982; 7:22-27.
18. King MA, Doherty PW, Rosenberg RJ, Cool SL. Array processors: an introduction to their architecture, software and applications in nuclear medicine. *J Nucl Med* 1983; 24:1072-1079.
19. King MA, Penney BC, Glick SJ. An image-dependent Metz filter for nuclear medicine images. *J Nucl Med* 1988; 29:1980-1989.
20. Budinger TF, Derenzo SE, Greenberg WL, Gullberg GT, Huesman RH. Quantitative potentials of dynamic emission computed tomography. *J Nucl Med* 1978; 19:309-315.
21. Hawkins WG, Yang NC, Lechner PK. Validation of the circular harmonic transform algorithm for quantitative SPECT. *J Nucl Med* 1990: in press.
22. Garcia E, Maddahi J, Berman D, Waxman A. Space/time quantitation of thallium-201 myocardial scintigraphy. *J Nucl Med* 1981; 22:309-317.
23. Garcia EV, Van Train K, Maddahi J, et al. Quantification of rotational thallium-201 myocardial tomography. *J Nucl Med* 1985; 26:17-26.